# Photon blockade in a Tavis-Cummings system

Brian Marinelli,[1,2,*] Alex H. Rubin,[3,4,*] Victoria A. Norman,[3,4] Santai Yang,[1] Ravi Naik,[1,2] Bethany M. Niedzielski,[5] David K. Kim,[5] Rabindra Das,[5] Mollie Schwartz,[5] David I. Santiago,[1,2] Christopher Spitzer,[1,2] Irfan Siddiqi,[1,2] and Marina Radulaski[3,†]

[1] *Quantum Nanoelectronics Laboratory, Department of Physics, University of California at Berkeley, Berkeley, California 94720, USA*

[2] *Computational Research Division, Lawrence Berkeley National Laboratory, Berkeley, California 94720, USA*

[3] *Department of Electrical and Computer Engineering, University of California, Davis, California 95616, USA*

[4] *Department of Physics, University of California, Davis, California 95616, USA*

[5] *Lincoln Laboratory, Massachusetts Institute of Technology, Lexington, Massachusetts 02421-6426, USA*

(Received 30 January 2025; revised 1 October 2025; accepted 6 October 2025; published 31 October 2025)

We observe blockade of microwave photons in a Tavis-Cummings system comprising a superconducting cavity and up to $N = 3$ transmon qubits. The effect is characterized with photon-number-resolving spectroscopy using an additional dispersively coupled transmon "witness" qubit to directly probe the cavity's photon-number distribution. We first observe polariton formation with splitting proportional to $\sqrt{N}$, confirming the Tavis-Cummings coupling, and subsequently obtain sub-Poissonian cavity photon statistics when the cavity is driven at polariton frequencies.

DOI: 10.1103/st87-3cxz

## I. INTRODUCTION

Photon-photon interactions are notoriously absent in nature except within media that exhibit optical nonlinearity—the phenomenology explored in classical and quantum optics alike. At the end of the twentieth century, scientists studied Kerr and Kerr-like nonlinearities for applications in photon logic and single-photon turnstile devices. Among these works was the theory of *photon blockade* (PB), where the absorption of one photon blocks the transmission of a subsequent photon [1]. Its experimental realizations in atomic, quantum dot, and superconducting Kerr and Jaynes-Cummings systems followed [2–5]. Next came observations of the unconventional PB in solid-state systems, which eased the conditions for demonstrating a PB effect toward weakly (as opposed to strongly) interacting oscillators [6,7]. Photon blockade has recently been proposed for Tavis-Cummings (TC) systems [8,9], which are of particular relevance for defect-related quantum emitters in semiconductors where strong cavity quantum electrodynamical (QED) coupling is currently achieved only with emitter ensembles [10–12].

The nature of PB in TC systems depends strongly on the relative detunings, loss rates, and coupling strengths of each emitter in the system. In solid-state experiments control over these values is generally coarse, making it challenging to systematically explore the large parameter space available. In this work we exploit the close analogy between cavity QED and circuit QED to implement many-body PB in a superconducting circuit, which provides fine-grained control of the Hamiltonian parameters. This serves as an analog simulation of the optical TC systems, enabling systematic exploration of parameter regimes that are challenging to access in conventional optical setups while providing valuable insights into the underlying many-body PB physics.

Photon blockade is typically manifested in terms of the statistics of photons emitted from the cavity, where the two-photon correlation function $g^{(2)}(\tau) < 1$ is used as an indicator of blockade. The correlation function can be measured with a Hanbury Brown-Twiss interferometer using a pair of photon detectors, which is especially straightforward in the optical domain where detectors are readily available and highly efficient [13]. In the microwave domain where photon detectors are less developed, correlation functions can be determined from quadrature measurements of the field leaking out of the cavity using homodyne or heterodyne detection [5,7,14]. These measurements require high-quality quantum-limited amplifiers

*These authors contributed equally.

†Contact author: mradulaski@ucdavis.edu

*Published by the American Physical Society under the terms of the Creative Commons Attribution 4.0 International license. Further distribution of this work must maintain attribution to the author(s) and the published article's title, journal citation, and DOI.*

to achieve high signal-to-noise ratio and can be very slow if high-order moments of the field distribution need to be measured. Recent work has used the more direct approach of coupling an auxiliary qubit to the cavity to perform Wigner tomography of the cavity state to verify PB [15,16]. If the qubit and cavity are coupled in the strong dispersive limit the cavity photon-number information can be mapped onto the qubit frequency.

In this work we use $N = 1, 2, 3$ superconducting transmon qubits capacitively coupled to a coplanar waveguide (CPW) cavity [17] to achieve the PB condition, observed in the cavity photon number. An additional transmon qubit in the strong-dispersive regime is used as a probe of the distribution of photon-number states in the cavity. We employ photon-number-resolving (PNR) spectroscopy [18,19] of this ancillary qubit to detect which photon-number states of the cavity are occupied in the presence and absence of PB. We show that as the blockading qubits are tuned into resonance with the cavity, the cavity occupation transitions from approximately Poissonian with up to $n = 4$ photons to sub-Poissonian occupation limited to only $n = 0, 1$. Our theoretical predictions explain the experimental data closely. These measurements constitute a simpler and more natural method for detection of PB in superconducting cavity QED systems in the microwave regime.

## II. PHOTON BLOCKADE

A cavity mode with frequency $\omega_c$ coupled to $N$ two-level quantum emitters with frequency $\omega_a$ is described by the TC Hamiltonian in the rotating wave approximation ($\hbar = 1$ here and throughout):

$$H_{\mathrm{TC}} = \omega_c a^\dagger a + \sum_i^N \left(\omega_a \sigma_i^+ \sigma_i^- + g(a^\dagger \sigma_i^- + a\sigma_i^+)\right), \quad (1)$$

where $a$ ($a^\dagger$) is the lowering (raising) operator for the cavity mode, $\sigma_i^-$ ($\sigma_i^+$) is the lowering (raising) operator for the $i$th emitter, and $g$ is the cavity-emitter coupling which we assume to be identical for all $N$ emitters.

In the strong-coupling regime, the eigenstates of $H$ are mixtures of light and matter known as polaritons. When the system is driven on-resonance with a polariton in the $n = 1$ subspace, the drive field is detuned from all 1-to-2 excitation transitions. Considering a coherent drive at the frequency of the lowest polariton ($\omega_d = \omega_c - \sqrt{N}g$), the detuning between $\omega_d$ and the transition to the nearest $n = 2$ state is $(2\sqrt{N} - \sqrt{4N-2})g$. If this detuning is large relative to $\kappa$ (the cavity linewidth) and $\gamma$ (the emitter linewidth), then the drive fails to significantly couple the $n = 1$ polariton to any state of the $n = 2$ manifold [see Fig. 1(d)].

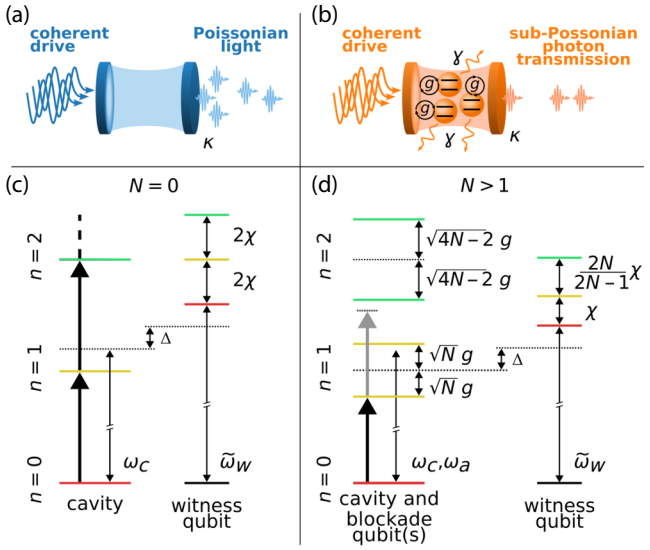



FIG. 1. (a) Illustration of an optical cavity driven by a coherent field. The photons transmitted through the cavity have Poissonian statistics, maintaining the coherent nature of the drive field. (b) Illustration of an open Tavis-Cummings system with three two-level emitters coupled to a cavity mode. The photons transmitted through the cavity have sub-Poissonian statistics due to photon blockade. (c) First few energy levels of an empty electromagnetic cavity (left) and a "witness" qubit dispersively coupled to the cavity (right). Dashed lines correspond to bare states. The witness qubit frequency shifts upward by $2\chi$ for each photon in the cavity. Spectroscopy of the witness qubit therefore reveals the cavity photon-number distribution. Thick arrows represent a coherent pump resonant with the first excited state of the cavity and therefore also with all higher transitions. (d) Left: highest and lowest levels of the first few excited-state manifolds of a system of $N$ identical qubits resonantly coupled to a cavity. Right: the corresponding energy levels of a witness qubit dispersively coupled to the same cavity. Dashed lines correspond to bare states. Thick arrows represent a coherent pump resonant with the lowest excited state, which is detuned from states in the $n = 2$ manifold, giving rise to photon blockade.

## III. PHOTON-NUMBER-RESOLVING SPECTROSCOPY

The photon-number statistics of the blockaded cavity can be extracted from the spectral response of a dispersively coupled qubit. This can be understood by again considering the Hamiltonian in Eq. (1) with $N = 1$ emitter, now termed the witness qubit, and working in the dispersive limit $g \ll \Delta_w = \omega_w - \omega_c$ where $\omega_w$ is the witness qubit frequency. A Schrieffer-Wolff transformation of that Hamiltonian yields

$$H_{\mathrm{disp}} = \omega_c a^\dagger a + \left(\tilde{\omega}_w + 2\chi a^\dagger a\right)\sigma^+\sigma^- \quad (2)$$

where $\tilde{\omega}_w = \omega_w + g^2/\Delta_w$ is the Lamb-shifted emitter frequency and

$$\chi = \frac{g^2}{\Delta_w\left(1 - \frac{\Delta_w}{\alpha}\right)} \tag{3}$$

for the transmon which is modified by the presence of higher levels from the usual $\chi_{\mathrm{TLS}} = g^2/\Delta_w$ for a pure two-level system . The interaction term can be viewed as a photon-number-dependent shift of the transmon frequency by $2\chi$ for every additional photon. The strong-dispersive regime is characterized by $\chi > \kappa, \gamma$ with $\kappa$ and $\gamma$ the cavity and qubit decay rates, respectively. In this limit it has been predicted [18] and observed [19] that the transmon response spectrum $S(\omega)$ will split into multiple resolvable peaks, separated by $2\chi$, corresponding to different numbers of photons in the cavity. The weights of the various peaks are approximately proportional to the probability of the corresponding photon number in the cavity. Therefore, measuring the qubit spectrum gives an estimate of the photon-number distribution in the cavity state.

## IV. EXPERIMENTAL RESULTS

We implement the TC model in a system consisting of eight flux-tunable transmon qubits capacitively coupled to a CPW resonator. The device is introduced and described in detail in Ref. [20]. The cavity frequency is $\omega = 5.230\,\mathrm{GHz}$, with cavity-emitter couplings $g = 12.5$–$13.7\,\mathrm{MHz}$ ($\bar{g} = 13.2\,\mathrm{MHz}$), emitter decay rates $\gamma \sim 0.1\,\mathrm{MHz}$, and cavity linewidth $\kappa = 0.1\,\mathrm{MHz}$. The coupling rates are extracted from fitting avoided crossings between the transmons and the cavity, like the one shown in Fig. 2(a). These avoided crossings are measured by using an on-chip flux line to tune the transmon frequency through the cavity frequency while performing two-tone spectroscopy on the transmon. This demonstrates that the transmons and cavity are in the strong coupling regime ($g \gg \kappa, \gamma$).

We begin by showing that PNR spectroscopy is an effective probe of PB by applying it to the Jaynes-Cummings system with $N = 1$ emitter blockading the cavity. Photon blockade in JC systems has been studied extensively in the past and serves as a benchmark of the method.

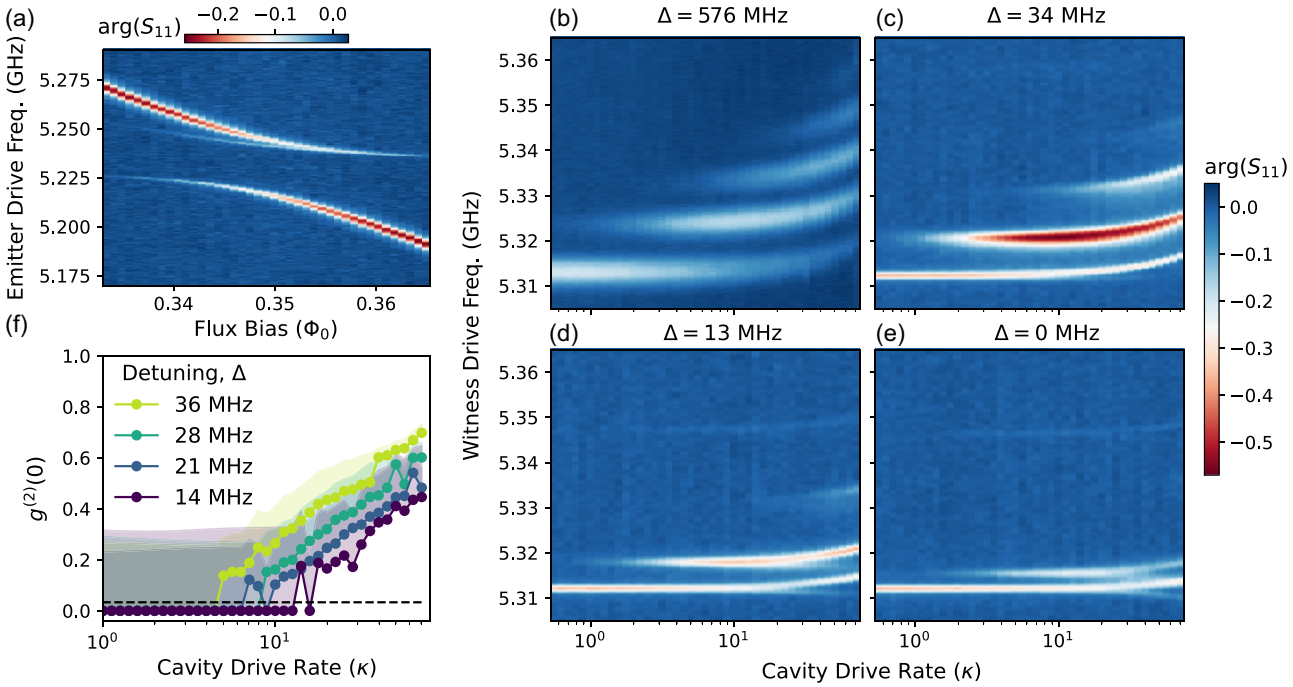



FIG. 2. Photon blockade in a Jaynes-Cummings system with strong coupling. (a) By varying the external magnetic flux the emitter transmon is tuned through an avoided crossing with the cavity from which we can extract the coupling $g = 13.7\,\mathrm{MHz}$ and the cavity-emitter polariton frequencies at various detunings, $\Delta$. Photon-number-resolving (PNR) spectroscopy is performed at cavity-emitter detunings (b) $\Delta = 43g = 576\,\mathrm{MHz}$, (c) $\Delta = 2.5g = 34\,\mathrm{MHz}$, (d) $\Delta = g = 13\,\mathrm{MHz}$, and (e) $\Delta = 0$ and drive amplitudes ranging from $\eta < \kappa$ to $\eta \gg \kappa$. Acquiring data for each of the four datasets took 24 minutes. The dim feature appearing at approximately 5.347 GHz in (d),(e) arises from an alternate transition in the $n = 1$ excitation manifold; see Appendix A for details. (f) As discussed in the text, these PNR spectra are used to estimate $g^{(2)}(0)$ as a function of cavity drive amplitude. The different colored points represent different cavity-emitter detunings, $\Delta$, which are specified in the legend. The shaded regions give error ranges on the measured $g^{(2)}(0)$ values according to the error analysis detailed in Appendix E 2. The dashed black line is the thermal limit for the minimum $g^{(2)}(0)$ given an estimate of 50 mK for the effective temperature of the cavity.

The witness transmon, $Q_w$, is tuned to $\omega_w = 5.313\,\mathrm{GHz}$ and has coupling to the cavity $g_w = 17\,\mathrm{MHz}$, detuning from the cavity $\Delta_w = \omega_w - \omega_c = 83\,\mathrm{MHz}$, and anharmonicity $\alpha = 227\,\mathrm{MHz}$. This leads to a dispersive shift of $\chi = 5.5\,\mathrm{MHz}$ which is easily resolved spectroscopically. A vector network analyzer is used to apply a weak readout tone to the readout resonator of the witness qubit and measure the relative amplitude and phase of the reflected signal ($S_{11}$), as a monitor of the qubit state. A weak probe tone is applied to the witness qubit charge drive line and swept across the bare qubit frequency and dispersively shifted qubit frequencies corresponding to up to $n = 4$ photons at $\omega_w + 8\chi$ to probe the qubit spectral response.

In the empty cavity limit where the emitter transmon is far off resonant with the cavity, $\Delta = 43g$, a drive resonant with the cavity frequency, $\omega_d = \omega_c$, is applied to the cavity drive line with varying amplitude. The resulting qubit spectrum is shown in Fig. 2(b). At very low powers a single peak in the spectrum is observed, corresponding to the bare qubit frequency. As the drive amplitude is increased the cavity is populated with nonzero average photon number, $\langle a^\dagger a\rangle > 0$, in steady state and the qubit spectrum shows additional peaks with relative shifts $2\chi$ corresponding to the dispersively shifted qubit frequency for different numbers of photons in the cavity. The relative weights of the peaks give an approximation of the photon-number distribution in the steady state at each drive amplitude.

Since $g_w/\Delta_w \approx 0.20$, there is some residual hybridization between the cavity and witness qubit which results in the measured photon-number distribution deviating from the expected Poisson distribution of a linear cavity excited by a classical drive. Despite this, peaks corresponding to photon numbers up to $n = 4$ are clearly observed. In Appendix E we compare the experimental results to simulations including and excluding the witness qubit to show that the presence of the witness qubit has a nonqualitative effect on the PB.

We repeat the PNR spectroscopy measurement at various detunings, $\Delta$, between an emitter transmon $Q_1$ and the cavity to show the emergence of the PB effect as the emitter transmon is brought into resonance with the cavity. The results are shown in Figs. 2(c)–2(e). At each detuning, the cavity is driven at the frequency of the cavitylike polariton (determined from the fit to the avoided crossing). We observe two important changes to the PNR spectrum of the witness qubit as the emitter-cavity detuning is reduced. First, the higher ($n > 1$) photon lines gradually fade and disappear until only the $n = 0, 1$ spectral features are left when the emitter and cavity are resonant ($\Delta = 0$) and the cavity photon number is blockaded. Further, we observe a reduction in the spacing between the $n = 0$ and $n = 1$ photon lines from $2\chi$ to $\chi$. This can be understood by noting that the polariton states have an average of $1/2$ photon when the emitter and cavity are resonant, $\langle \pm|a^\dagger a|\pm\rangle = 1/2$, so the resulting dispersive shift on the witness qubit when they are excited is halved. In general, the shift is approximately proportional to the weight of the cavitylike part of the polariton at each detuning. More details can be found in Appendix A.

We also note a feature in the witness qubit spectrum near 5.35 GHz that moves down slightly as the cavity-emitter detuning is reduced. This feature arises due to the coupling of the witness qubit to the rest of the system. If the witness qubit's coupling was perfectly dispersive, then when the blockade qubit is on-resonance, the coherent drive would populate $|-\rangle$, the lower polariton state. PNR spectroscopy would observe flips of the witness alone: $|-\rangle|g\rangle_w \to |-\rangle|e\rangle_w$. However, coherent coupling of the witness distorts the eigenstates of the blockade part of the system so that the lower polaritonlike state is $|\tilde{-}\rangle \neq |-\rangle$, so PNR spectroscopy also uncovers transitions to the upper polaritonlike state: $|\tilde{-}\rangle|g\rangle_w \to |\tilde{+}\rangle|e\rangle_w$, which is visible as the 5.35 GHz line. See Appendix A for more details.

Photon blockade is typically demonstrated by a low value (less than 1) of the two-photon correlation function

$$g^{(2)}(0) = \frac{\langle a^\dagger a^\dagger a a\rangle}{\langle a^\dagger a\rangle^2}. \tag{4}$$

By estimating the cavity occupation distribution from the PNR spectrum we can compute $g^{(2)}(0)$ (see Appendix E for more details) at each emitter-cavity detuning, shown in Fig. 2(f), at a variety of cavity drive amplitudes. We observe two important features of PB in JC systems. As the drive strength is increased, the PB gradually weakens as the driving rate overcomes the detuning between the polariton frequency and the frequencies of 1-to-2 excitation transitions in the system. Consequently, as the emitter is tuned off-resonant with the cavity this detuning is reduced and the blockade breaks down at successively lower drive strengths.

Having validated the PNR technique in the case of a JC system, we now apply it to TC systems with $N = 2$ and $N = 3$ emitter transmons. We begin by probing the dependence of the collective coupling on the number of emitters in the TC system. All emitters are tuned into resonance with the cavity ($\Delta = 0$) and we fix the cavity drive amplitude at $\eta = 10\kappa$ while sweeping the cavity drive frequency across the polariton frequencies at $\omega_c \pm \sqrt{N}g$. The resulting PNR spectra in Figs. 3(a) and 3(b) reveal $n = 1$ photon features when the cavity is driven near the polariton frequencies and the measured polariton splitting follows the expected $\sqrt{N}$ dependence [21].

Next we fix the cavity drive frequency at the lower polariton frequency and sweep the cavity drive amplitude [similar to the measurement in Fig. 2(e)]. Only the $n = 0$ and $n = 1$ photon features are observed in the PNR spectra [Figs. 3(c) and 3(d)], thus demonstrating the observation of PB in the TC systems with both $N = 2$ and $N = 3$ emitters.

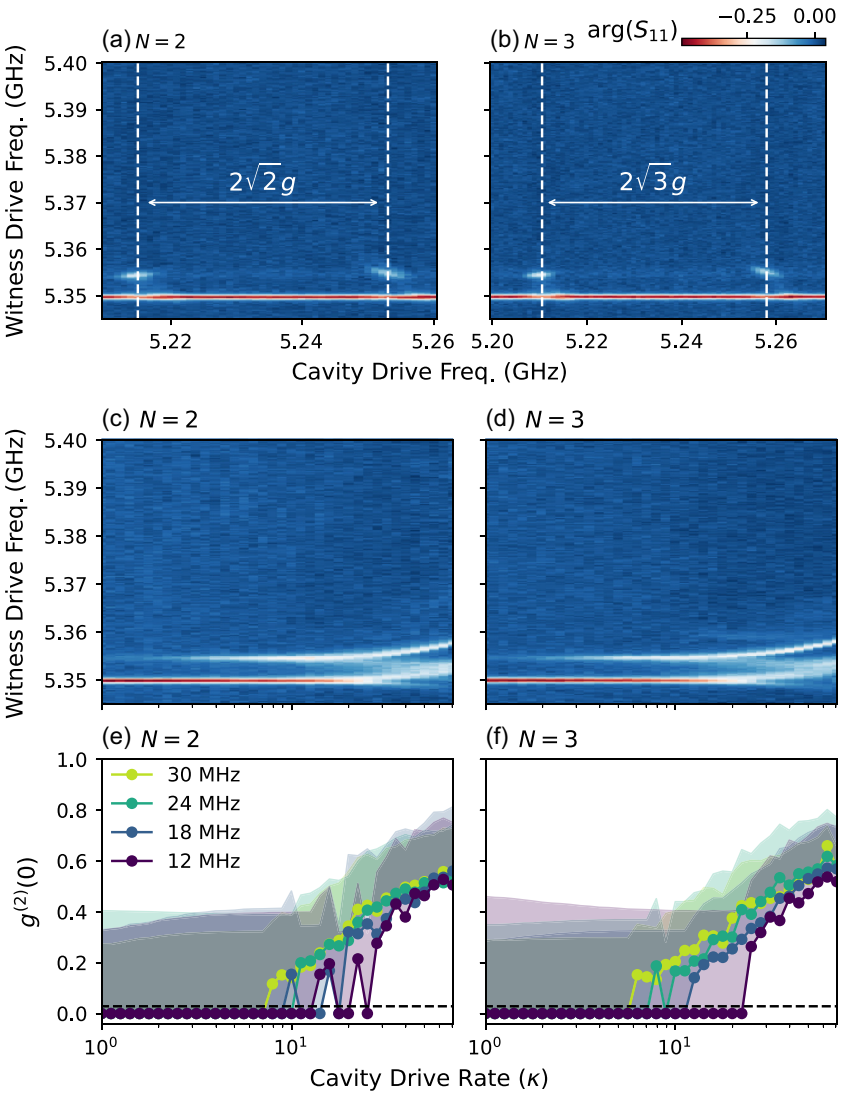



FIG. 3. Observation of photon blockade in Tavis-Cummings systems. PNR spectrum with (a) $N = 2$ and (b) $N = 3$ emitter transmons tuned into resonance with the cavity. The spectrum is measured with fixed cavity drive amplitude $\eta = 10\kappa$ while sweeping the cavity drive frequency across the polariton frequencies. Vertical dashed lines mark the polariton frequencies with splitting $2g_{\mathrm{col}} \approx 2\sqrt{N}\bar{g}$. The PNR spectrum for (c) $N = 2$ and (d) $N = 3$ as a function of the drive amplitude with drive frequency fixed at the lower polariton frequency. The $g^{(2)}(0)$ is extracted for (e) $N = 2$ and (f) $N = 3$ by repeating the above measurements at various cavity-emitter detunings. The shaded regions give error ranges on the measured $g^{(2)}(0)$ values according to the error analysis detailed in Appendix D. The dashed black line is the thermal limit for the minimum $g^{(2)}(0)$ given an estimate of 50 mK for the effective temperature of the cavity.

Again, we extract $g^{(2)}(0)$ across a wide range of cavity-emitter detunings and cavity drive amplitudes, observing a dependence similar to the JC case [Figs. 3(e) and 3(f)]. As expected, the PB breaks down at large detunings and large drive amplitudes where the drive is able to excite the system beyond the $n = 1$ excitation manifold [22].

## V. DISCUSSION

Nonclassical states of light, particularly single photons, are essential resources for technologies such as quantum communication, quantum computation [23], and quantum sensing [24]. The ability to generate and manipulate these states with high fidelity and efficiency is a major hurdle to realizing the full potential of quantum technologies. Photon blockade presents one well-known avenue for imprinting the inherent nonclassicality of a two-level quantum system onto an optical mode.

In this work, we performed analog simulations of many-body PB by implementing the TC Hamiltonian in a superconducting circuit. Using PNR spectroscopy, we observed PB in a circuit QED system containing up to $N = 3$ transmon qubits. This observation is confirmed by the vanishing of the PNR peaks for photon numbers greater than 1 when $N = 1, 2, 3$ transmons are tuned onto resonance with the cavity for blockade, and by the $\sqrt{N}$ scaling of the separation between the polaritons in the single-excitation manifold.

The PNR spectrum of the witness qubit at a particular cavity-emitter detuning and cavity drive amplitude was measured in 32 seconds. Multiple $n$th-order correlations can be calculated from this data quickly in postprocessing following Eq. (E2) in Appendix E. In comparison, similar measurements in quantum dot-cavity JC systems take seconds, minutes, and hours for $g^{(2)}$, $g^{(3)}$, and $g^{(4)}$ correlations, respectively [25]. Thus, this technique offers

shorter measurement times when compared to optical systems using photodetectors. These faster measurement times come at the expense of reduced sensitivity to very small values of the correlation function, $g^{(2)}(0) \ll 1$. Furthermore, the strong dispersive coupling easily achieved in these systems, combined with the ability to directly probe the "witness" qubit, circumvents the need for highly efficient single-photon detectors required in optical experiments, which are not readily available at microwave energies.

Understanding PB in TC systems is critical because real-world optical quantum devices often naturally feature multiple emitters. It is generally assumed that PB is inhibited in multiemitter systems as increasing the number of emitters reduces the effective nonlinearity of the system. Our work demonstrates that strong PB persists even in the case of multiple quantum emitters. Recent theoretical work on such systems has shown that the PB effect can even be enhanced in certain cases by adding more emitters to the cavity [9]. Another proposal suggests adding a second detuned cavity mode to preserve large transmission and strong blockade at large numbers of emitters [26].

The high degree of control and flexibility afforded by superconducting circuits makes them an attractive platform for exploring these different aspects of blockade physics with many emitters. We demonstrate this flexibility by tuning the emitter frequencies *in situ* to systematically study conventional PB as a function of cavity-emitter detuning. This analog simulation approach bridges the gap between superconducting quantum circuits and traditional optical cavity QED, providing insights into many-body quantum optical phenomena that are relevant for future quantum optical technologies but difficult to explore directly in conventional optical platforms. The combination of strong photon-photon interactions and high degree of tunability in this platform may allow for the investigation of more exotic regimes of PB such as unconventional [6] and subradiant blockade [8].

The successful observation of PB using PNR spectroscopy in superconducting circuits also opens up new possibilities for studying and comparing blockade physics across different platforms. While optical and superconducting systems have distinct advantages and challenges, valuable insights may be gained from comparing the two. For example, the ability to engineer and control interactions in superconducting architectures could provide a means to simulate and study blockade phenomena that are challenging to access in optical systems. By comparing the blockade behavior and its dependence on system parameters across these different platforms, we may gain a deeper understanding of the fundamental physics and identify new avenues for enhancing the performance of blockade-based single-photon sources in both optical and microwave domains.

## ACKNOWLEDGMENTS

The authors acknowledge support by Noyce Foundation, National Science Foundation CAREER program (Award No. 2047564), the UC Multicampus Research Programs and Initiatives of the University of California (Grant No. M23PL5936). This material was funded in part by the US Department of Energy, Office of Science, Office of Advanced Scientific Computing Research Quantum Testbed Program under contracts DE-AC02-05CH11231. This paper describes objective technical results and analysis. Any subjective views or opinions that might be expressed in the paper do not necessarily represent the views of the US Department of Energy or the United States Government.

## DATA AVAILABILITY

The data that support the findings of this article are openly available [27].

## APPENDIX A: EFFECTIVE DISPERSIVE SHIFT

We derive analytically the dispersive shift of the witness qubit for each occupation state of the resonant cavity with blockade qubit(s).

### 1. $N = 1$ blockade qubit

We consider the case of $N = 1$ blockade qubits first as the simplest example. There are two cases to consider: $n = 1$ and $n > 1$ excitations. The $n = 1$ excited manifold is spanned by the basis $\{|1,g,g\rangle, |0,e,g\rangle, |0,g,e\rangle\}$, where the three entries of each state label the cavity photon number, the blockade qubit state, and the witness qubit state, respectively. In this basis, the Hamiltonian is given by

$$H = \begin{pmatrix} \omega_c - \chi & g & 0 \\ g & \omega_a & 0 \\ 0 & 0 & \omega_w + \chi \end{pmatrix}.$$

The upper left block corresponds to the subspace where the witness qubit is in $|g\rangle$. The eigenstates of this block are

$$\begin{aligned} |\psi^{g\pm}_{N=1,n=1}\rangle &= -\frac{1}{2g}\left(\Delta + \chi \pm \sqrt{4g^2 + (\Delta+\chi)^2}\right)|1,g,g\rangle \\ &\quad + |0,e,g\rangle, \end{aligned}$$

where $\Delta \equiv \omega_a - \omega_c$ and we have ignored normalization for readability. These states have energies

$$E^{g\pm}_{N=1,n=1} = \frac{1}{2}\left(\omega_a + \omega_c - \chi \pm \sqrt{4g^2 + (\Delta+\chi)^2}\right)$$

and correspond to the familiar $n = 1$ polaritons of the Jaynes-Cummings Hamiltonian, plus a dispersive shift.

The lower right block of the $n = 1$ Hamiltonian corresponds to the single excitation residing in the witness qubit,

$$|\psi^{e}_{N=1,n=1}\rangle = |0, g, e\rangle,$$

which has energy

$$E^{e}_{N=1,n=1} = \omega_w + \chi.$$

In the $n > 1$ excitation case, using the basis $\{|n, g, g\rangle, |n-1, e, g\rangle, |n-1, g, e\rangle, |n-2, e, e\rangle\}$, the Hamiltonian is given by

$$H = \begin{pmatrix} n(\omega_c - \chi) & g\sqrt{n} & 0 & 0 \\ g\sqrt{n} & (n-1)(\omega_c - \chi) + \omega_a & 0 & 0 \\ 0 & 0 & (n-1)(\omega_c + \chi) + \omega_w + \chi & g\sqrt{n-1} \\ 0 & 0 & g\sqrt{n-1} & (n-2)(\omega_c + \chi) + \omega_w + \chi + \omega_a \end{pmatrix}.$$

Again, the upper left block corresponds to states analogous to $n$-excitation Jaynes-Cummings polaritons (again ignoring normalization),

$$|\psi^{g\pm}_{N=1,n>1}\rangle = -\frac{1}{2\sqrt{n}g}\left(\Delta + \chi \pm \sqrt{4g^2 n + (\Delta + \chi)^2}\right)|n, g, g\rangle + |n-1, e, g\rangle,$$

with corresponding energies

$$E^{g\pm}_{N=1,n>1} = \frac{1}{2}\left(\omega_a + (2n-1)(\omega_c - \chi) \pm \sqrt{4g^2 n + (\Delta + \chi)^2}\right).$$

The lower left block also represents states similar to Jaynes-Cummings type polaritons, now with $n-1$ excitations in the polariton part and one excitation in the witness:

$$|\psi^{e\pm}_{N=1,n>1}\rangle = -\frac{1}{2\sqrt{n-1}g}\left(\Delta + \chi \pm \sqrt{4g^2(n-1) + (\chi - \Delta)^2}\right) \times |n-1, g, e\rangle + |n-2, e, e\rangle$$

(where we have again ignored normalization) with corresponding energies

$$E^{e\pm}_{N=1,n>1} = \frac{1}{2}\left(\omega_a + (2n-3)\omega_c + 2\omega_w + (2n-1)\chi \pm \sqrt{4g^2(n-1) + (\chi - \Delta)^2}\right).$$

We now map out the PNR transitions of the witness qubit. From here on we consider the blockade qubits to be on-resonance with the cavity so that $\Delta = 0$. Assume the system starts in its ground state $|0, g, g\rangle$. When the witness qubit is probed, if it is flipped to $|e\rangle$, the system moves to $|\psi^{e}_{N=1,n=1}\rangle$, with energy $\omega_w + \chi$, reflecting the Lamb shift of the witness. If the system instead starts in an $n$-excitation polaritonlike state $|\psi^{g\pm}_{N=1,n>0}\rangle$ where the witness is in $|g\rangle$, then exciting the witness qubit couples the system to states in the $(n+1)$-excitation manifold:

$$\langle\tilde{\psi}^{e\pm}_{N=1,n+1}|\sigma^{x}_{w}|\tilde{\psi}^{g\pm}_{N=1,n>0}\rangle = \frac{2\sqrt{n}g}{\sqrt{4ng^2 + \chi^2}} \approx 1, \quad \text{(A1)}$$

$$\langle\tilde{\psi}^{e\mp}_{N=1,n+1}|\sigma^{x}_{w}|\tilde{\psi}^{g\pm}_{N=1,n>0}\rangle = \pm\frac{\chi}{\sqrt{4ng^2 + \chi^2}} \approx 0, \quad \text{(A2)}$$

where $\sigma^{x}_{w}$ is the Pauli X operator acting on the witness qubit, the tildes indicate normalization, and the approximation is made in the limit $\chi \ll g$. So when the cavity and blockade qubit contains $n$ excitations, the witness qubit can be flipped when addressed with energy

$$E^{e\pm}_{N=1,n+1} - E^{g\pm}_{N=1,n} = \omega_w + 2n\chi.$$

The fact that the witness qubit can be flipped without changing the state of the rest of the system means that we can also obtain the PNR spectrum of the witness by considering the eigenstates of the blockade portion of the system in isolation:

$$\omega_w + (1 + 2\langle\psi_{N=1,n}|a^{\dagger}a|\psi_{N=1,n}\rangle)\chi = \omega_w + 2n\chi,$$

where $|\psi_{N=1,n}\rangle$ is the eigenstate of an ordinary JC system with $n$ excitations (without the witness).

We also note that the small effect of the witness can also be observed by the differences between the eigenenergies with ($E^{g\pm}_{N=1,n}$) and without ($E^{\pm}_{N=1,n}$) the witness qubit. Using our experimental parameters (given in the main text), when

the system is resonant ($\omega_a = \omega_c$, $\Delta = 0$), we have

$$\begin{aligned}\Delta_{\text{with witness}} &= E^{g\pm}_{N=1,n+1} - E^{g\pm}_{N=1,n>0} \\ &= \omega_c - \chi - \frac{1}{2}\sqrt{4ng^2 + \chi^2} \\ &\quad + \frac{1}{2}\sqrt{4g^2(n+1) + \chi^2}. \\ \Delta_{\text{without witness}} &= E^{\pm}_{N=1,n+1} - E^{\pm}_{N=1,n>0} \\ &= \omega_c - \frac{1}{2}\sqrt{4ng^2} + \frac{1}{2}\sqrt{4g^2(n+1)},\end{aligned}$$

so that

$$\begin{aligned}&\Delta_{\text{without witness}} - \Delta_{\text{with witness}} \\ &\quad = \chi + g(\sqrt{n+1} - \sqrt{n}) + \frac{1}{2}\sqrt{4g^2 n + \chi^2} \\ &\qquad - \frac{1}{2}\sqrt{4g^2(n+1) + \chi^2} \approx \chi,\end{aligned}$$

where the final approximation holds when $\chi \ll \sqrt{n}g$, as is true of our system. Thus, the effect of the witness on the blockade system is to reduce the energy required to add an excitation to the system by roughly $\chi$, which for our experimental parameters is about 5.5 MHz, or about $\chi/\omega_c = (5.5\,\text{MHz})/(5.230\,\text{GHz}) \approx 0.1\%$.

### 2. $N > 1$ blockade qubits, $n = 1$ excitations

For $N = \{2, 3\}$, a similar (albeit tedious) analysis shows that the approximations (A1) and (A2) hold when $\chi \ll \sqrt{N}g$. We omit this derivation and focus on the resulting PNR shifts of the witness qubit, which we compute directly from the mean photon number of the relevant eigenstates of the blockade system without the witness qubit, as discussed above.

Since we focus only on the case of resonant, identical blockade qubits, we simplify matters by working in the basis of collective states, where $N$ spin-1/2 systems are considered to act as a single spin-$N/2$ system. Regardless of $N$, the basis $\{|1, -N/2\rangle, |0, -N/2+1\rangle\}$ spans the single-excitation manifold. In this basis we have

$$H = \begin{pmatrix} n\omega_c & \sqrt{N}g \\ \sqrt{N}g & (n-1)\omega_c + \omega_a \end{pmatrix},$$

with polaritonlike eigenstates (ignoring normalization)

$$\begin{aligned}&|\psi^{\pm}_{N>1,n=1}\rangle \\ &\quad = -\frac{1}{2\sqrt{N}g}\left(\Delta + \chi \pm \sqrt{4Ng^2 + (\Delta+\chi)^2}\right)|1, g, g\rangle \\ &\qquad + |0, e, g\rangle.\end{aligned}$$

Considering the resonant case $\omega_a = \omega_c$, straightforward calculation gives

$$(1 + 2\langle\tilde{\psi}^{\pm}_{N>1,n=1}|a^\dagger a|\tilde{\psi}^{\pm}_{N>1,n=1}\rangle)\chi = 2\chi,$$

where the tildes indicate normalization.

### 3. $N = 2$ blockade qubits

With the $n = 1$ case covered by the foregoing, we can immediately move to $n > 1$, where we have

$$H = \begin{pmatrix} n\omega_c & \sqrt{2n}g & 0 \\ \sqrt{2n}g & (n-1)\omega_c + \omega_a & \sqrt{2(n-1)}g \\ 0 & \sqrt{2(n-1)}g & (n-2)\omega_c + 2\omega_a \end{pmatrix}.$$

There are now more than two eigenstates; we consider only the highest and lowest (denoted by $\pm$), since these are the states most likely to be involved in multiphoton events when the system is driven on-resonance with either of the $n = 1$ eigenstates. As before, setting $\omega_c = \omega_a$, we compute

$$\begin{aligned}&\left(1 + 2\langle\tilde{\psi}^{\pm}_{N=2,n>1}|a^\dagger a|\tilde{\psi}^{\pm}_{N=2,n>1}\rangle\right)\chi \\ &\quad = \left(2n - 1 + \frac{1}{2n-1}\right)\chi,\end{aligned}$$

which agrees with the $n = 1$ case as well.

### 4. $N = 3$ blockade qubits

We must consider two special cases: $n = 2$ and $n > 2$.

#### *a. $n = 2$ excitations*

The Hamiltonian is given by

$$H = \begin{pmatrix} 2\omega_c & \sqrt{6}g & 0 \\ \sqrt{6}g & \omega_c + \omega_a & 2g \\ 0 & 2g & 2\omega_a \end{pmatrix}.$$

Again, setting $\omega_c = \omega_a$, we compute

$$\left(1 + 2\langle\tilde{\psi}_{N=3,n=2}|a^\dagger a|\tilde{\psi}_{N=3,n=2}\rangle\right)\chi = 3.2\chi$$

#### *b. $n > 2$ excitations*

The Hamiltonian is now given by

$$H = \begin{pmatrix} n\omega_c & \sqrt{3n}g & 0 & 0 \\ \sqrt{3n}g & (n-1)\omega_c + \omega_a & 2\sqrt{n-1}g & 0 \\ 0 & 2\sqrt{n-1}g & (n-2\omega_c) + 2\omega_c & \sqrt{3(n-2)}g \\ 0 & 0 & \sqrt{3(n-2)}g & (n-3)\omega_c + 3\omega_a \end{pmatrix}.$$

Again, setting $\omega_c = \omega_a$, we compute

$$(1 + 2\langle\tilde{\psi}^{\pm}_{N=3,n>2}|a^\dagger a|\tilde{\psi}^{\pm}_{N=3,n>2}\rangle)\chi = \left(2n - 2 + \frac{6}{\sqrt{16n(n-2)+25}}\right)\chi,$$

which agrees with the $n = \{1, 2\}$ cases as well.

#### 5. $N > 1$ blockade qubits, $n = 2$ excitations

When blockade is in effect, only the $n = 0$ and $n = 1$ lines will appear in the PNR spectrum. The positions of both those lines as a function of $N$ in the general case are given in the foregoing. We now give the position of the $n = 2$ line (the first line suppressed by blockade) as a function of $N$. The Hamiltonian is given by

$$H = \begin{pmatrix} 2\omega_c & \sqrt{2n}g & 0 \\ \sqrt{2n}g & \omega_c + \omega_a & \sqrt{2n-2}g \\ 0 & \sqrt{2n-2}g & 2\omega_a \end{pmatrix}.$$

On resonance ($\omega_a = \omega_c$) we find for the upper and lower states $\psi^{\pm}_{N>1,n=2}$,

$$(1 + 2\langle\psi^{\pm}_{N>1,n=2}|a^\dagger a|\psi^{\pm}_{N>1,n=2}\rangle)\chi = \frac{6N-1}{2N-1}\chi$$

so that the shift from the $n = 1$ level to the $n = 2$ level is

$$\frac{6N-1}{2N-1}\chi - 2\chi = \frac{2N}{2N-1}\chi,$$

which agrees with the $N = 1$ case as well.

#### 6. Intuition

These results can be understood as follows. The first excitation of the cavity and blockade qubit(s) is exactly half cavitylike regardless of $N$, because there is only one way to split a single excitation between the cavity and the qubit(s). Therefore populating this state shifts the witness qubit by $\chi$. When a second excitation is added to the cavity and blockade qubit(s), the number of ways to distribute this excitation depends on the number of blockade qubit(s) $N$. For $N = 1$, the blockade qubit is already saturated and so each additional excitation is purely cavitylike, shifting the witness a further $2\chi$. For small $N > 1$, the blockade qubits are partially but not completely filled by the first excitation, and so the second excitation is partly in the cavity, partly in the qubits. For large TC systems ($N \gg 1$) the collective state space of the blockade qubits becomes effectively harmonic, and so each additional excitation is equally shared between cavity and blockade qubit(s), so the dispersive shift of the witness tends to $\chi$ per excitation as $N \to \infty$. For any finite $N$, as $n \to \infty$ the blockade qubits become saturated, and each additional excitation asymptotically resides purely in the cavity, so subsequent dispersive shifts of the witness tend toward $2\chi$.

## APPENDIX B: DRIVE AMPLITUDE CALIBRATION

In this section we describe the protocol used to calibrate the ratio between the source drive amplitude in volts and the drive rate $\eta$ of the cavity. As described in the main text, when a qubit is tuned on-resonance with the cavity there is a conventional photon blockade effect, preventing the system from being excited to beyond the single-excitation manifold spanned by the polariton states $|\pm\rangle$. For sufficiently small drive amplitudes, $\eta \ll g$, we can isolate the vacuum state and one of the polaritons to form a two-level system (TLS), $\{|0\rangle, |\pm\rangle\}$. Then we note that

$$\langle 0|\eta(a + a^\dagger)|-\rangle = \langle 0|\eta(a + a^\dagger)|+\rangle = \frac{1}{2}\eta, \tag{B1}$$

or more generally, if the qubit and cavity are nearly on-resonance, $0 < \Delta \ll g$, we still have

$$\langle 0|\eta(a + a^\dagger)|-\rangle + \langle 0|\eta(a + a^\dagger)|+\rangle = \eta. \tag{B2}$$

Thus, for a given drive voltage amplitude, $V$, we can extract $\eta(V)$ from the Rabi oscillation rates of the TLS spanned by the vacuum and the polaritons under resonant driving. We tune $Q_5$ onto resonance with the cavity and drive the system resonantly with each polariton frequency while sweeping the drive amplitude. The resulting Rabi rates are extracted from fitting the qubit population oscillations to a sinusoid with a decaying envelope to account for decoherence.

The extracted Rabi rates for both polaritons are shown in Fig. 4. The linear fit used to extract the drive strength to voltage amplitude ratio uses the first four data points and excludes the highest-amplitude results which deviate from the linear trend.

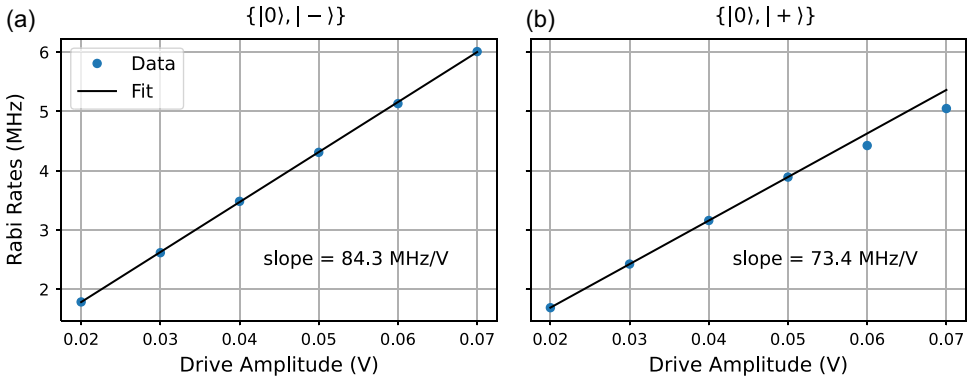



FIG. 4. Lower (a) and upper (b) polariton Rabi rates versus drive amplitude. Rabi rates (blue dots) are extracted from fitting experimentally measured $Q_5$ population oscillations while resonantly driving at the polariton frequencies. Linear fit (black line) gives the Rabi rate to drive amplitude ratio in megahertz per volt.

## APPENDIX C: EXPERIMENTAL SETUP

In Fig. 5 we show the room-temperature microwave setup used for the measurements throughout the main text. Details of the cryogenic wiring can be found in the Supplemental Material of Ref. [20]. A Keysight N5241B vector network analyzer (VNA) is used to continuously measure the readout signal, $S_{11}$, with a weak probe tone applied from Port 1 and the reflected signal returned at port 2. The extra rf source, SRC, from the VNA is used to apply a weak drive on the witness qubit to probe its spectral response. A separate rf source, AnaPico Aspin20G, is used to drive the cavity. The cavity drive passes through a power combiner to enable measurements where the cavity is driven simultaneously by multiple tones (not presented in this work).

## APPENDIX D: NUMERICAL SIMULATION WITH QUTIP

To simulate this situation, we add a coherent drive term

$$H_{\text{drive}} = \eta a^\dagger e^{-i\omega_d t} + \text{h.c.} \tag{D1}$$

to form the Hamiltonian $H = H_{\text{TC}} + H_{\text{drive}}$, where $\omega_d$ is the drive frequency and $\eta$ is the drive field amplitude (in units of frequency; photons per unit time). The time dependence is removed by unitary transformation into a frame corotating with the drive tone:

$$\begin{aligned}\tilde{H} &= U^\dagger H U - iU\frac{dU}{dt} \\ &= \Delta\hat{n} + g\sum_i^N \left(a^\dagger\sigma_i^- + a\sigma_i^+\right) + \eta(a^\dagger + a),\end{aligned}$$

where $U = \exp(i\omega_d\hat{n}t)$ and $\Delta \equiv \omega - \omega_d$ is the detuning of the drive.

Loss of excitations to the environment is assumed to be Markovian, so we write a master equation for the overall dynamics of the system in Lindblad form as

$$\dot{\rho} = -i[\tilde{H}, \rho] + \mathcal{D}_a(\rho) + \sum_i^N \mathcal{D}_{\sigma_i^-}(\rho), \tag{D2}$$

where

$$\mathcal{D}_A(\rho) \equiv A\rho A^\dagger - \frac{1}{2}\left\{A^\dagger A, \rho\right\}_+ \tag{D3}$$

is the Lindblad dissipator generated by the operator $A$, so that $\mathcal{D}_a$ and $\mathcal{D}_{\sigma_i^-}$ represent losses to the environment via the cavity and via the $i$th emitter, respectively.

Our experimental measurements represent averages over periods much longer than the characteristic timescales of the system $(\omega, g, \kappa, \gamma)$, so we deal exclusively with expectation values and correlation functions of the steady state ($\dot{\rho}_{\text{ss}} = 0$), which we obtain by solving Eq. (D2) using the python package QuTiP.

Photon blockade is typically characterized by low values (below 0.5) of the two-photon correlation function

$$g^{(2)}(0) = \frac{\langle a^\dagger a^\dagger a a\rangle}{\langle a^\dagger a\rangle^2}, \tag{D4}$$

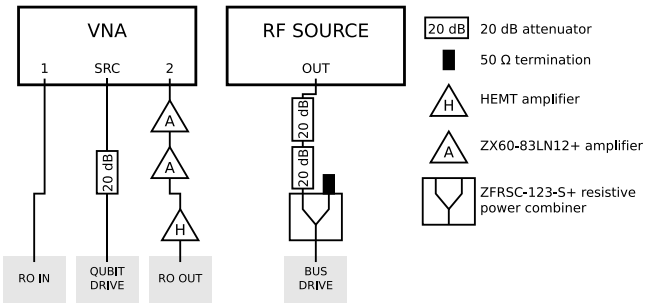



FIG. 5. Room temperature wiring diagram for measurements throughout the main text.

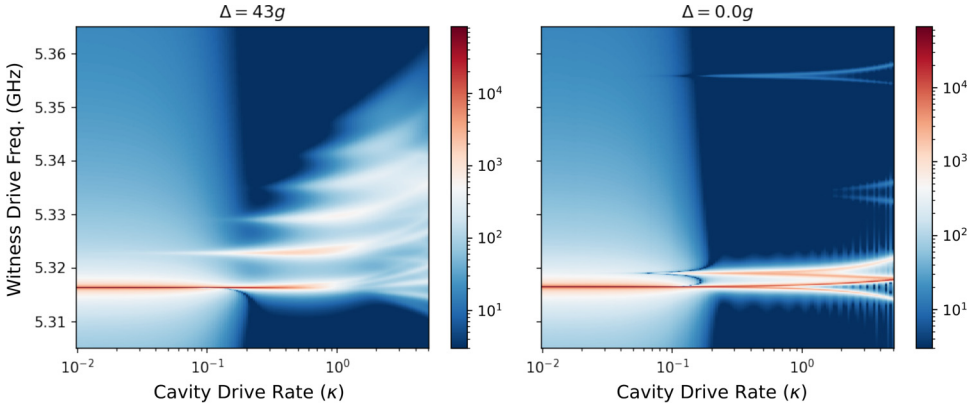



FIG. 6. Simulation of the spectrum of the witness qubit $S_{\sigma_x}(\omega)$ as a function of cavity drive power, for a system containing a single blockade qubit. On the left, the blockade qubit is far detuned ($\Delta \gg g$) from the cavity; on the right, the blockade qubit is resonant with the cavity.

which has the virtue of being straightforwardly implemented in the optical domain in terms of a photon counting experiment. While this is a measurement on photons emitted from the cavity, in simulation we can compute $g^{(2)}(0)$ using the cavity annihilation operator $a$, since the number of photons emitted from the cavity is proportional to the cavity occupation.

In this work, we use PNR spectroscopy to observe photon blockade—directly probing the photon-number distribution of the cavity. In this case, blockade is evidenced by a divergence of the photon-number distribution from the well-known Poisson distribution that represents the steady state of a bare cavity under coherent drive. In Fig. 6 we compare an example simulation of the steady-state photon-number distributions within two coherently pumped cavities (one bare, one containing a resonant emitter creating a blockade). The blockaded system shows dramatically attenuated occupation of higher (greater than 1) Fock states, and clearly diverges from the Poisson distribution which has the same average photon number.

## APPENDIX E: EXTRACTING $g^{(2)}(0)$ FROM PNR SPECTRA

### 1. Estimating $g^{(2)}(0)$

The second-order correlation function used as an indicator of photon blockade,

$$g^{(2)}(0) = \frac{\langle a^\dagger a^\dagger a a \rangle}{\langle a^\dagger a \rangle^2} = \frac{\sum_{n=0}^{\infty} n(n-1)P(n)}{\left[\sum_{n=0}^{\infty} nP(n)\right]^2}, \tag{E1}$$

can be computed from the photon-number distribution in the cavity, $P(n)$. Here we outline the procedure for estimating $P(n)$ from the experimentally measured PNR spectra. First, we find the peaks in the witness qubit spectrum [Fig. 7(a)]. The peak heights are taken as the weights, $W_n$, of the corresponding photon number $n$ in the distribution [Fig. 7(b)]. We normalize the distribution so that $P(n) = W_n/(\sum_n W_n)$ and $\sum_n P(n) = 1$. Finally, we plug these $P(n)$ into Eq. (E1) to estimate $g^{(2)}(0)$ at each cavity drive amplitude [Fig. 7(c)]. This procedure is repeated as we vary the cavity-emitter detunings and the number of emitters, $N$.

Since the PNR technique obtains information about the photon distribution directly, we can in principle also compute higher level-correlations,

$$g^{(m)}(0) = \frac{\sum_{n=0}^{\infty}\left(\prod_{i=0}^{m-1}(n-i)\right)P(n)}{\left[\sum_{n=0}^{\infty} nP(n)\right]^m}. \tag{E2}$$

### 2. Error analysis

We consider three main error sources to compute the shaded regions in Figs. 2 and 3 in the main text.

First, we estimate the effect of the residual hybridization of the witness qubit with the cavity and the emitters. To evaluate this source of error we consider the details of the witness qubit dispersive measurement. The witness qubit is dispersively coupled to a readout resonator with dispersive shift $\chi_{\mathrm{RO}}$. We monitor the reflected signal, $S_{11}$, of a microwave tone near the readout resonator frequency. Since we average over long times with the system in steady state, the measured complex reflection response is given by

$$S_{11}(\omega) = \frac{\omega - \omega_{\mathrm{RO}}(\langle\sigma_z\rangle) + \frac{i}{2}\kappa_{\mathrm{RO}}}{\omega - \omega_{\mathrm{RO}}(\langle\sigma_z\rangle) - \frac{i}{2}\kappa_{\mathrm{RO}}} \tag{E3}$$

centered at $\omega_{\mathrm{RO}}(\langle\sigma_z\rangle) = \omega_{\mathrm{RO},0} + \langle\sigma_z\rangle\,\chi_{\mathrm{RO}}$, where $\langle\sigma_z\rangle$ is the steady-state expectation value of the witness qubit $\sigma_z$ Pauli operator and $\kappa_{\mathrm{RO}}$ is the readout resonator linewidth. If we fix the readout tone near the ground-state frequency, $\omega_{\mathrm{RO},0} + \chi$, in the limit where $\chi < \kappa_{\mathrm{RO}}$ (the dispersive shift is smaller than the readout resonator linewidth)

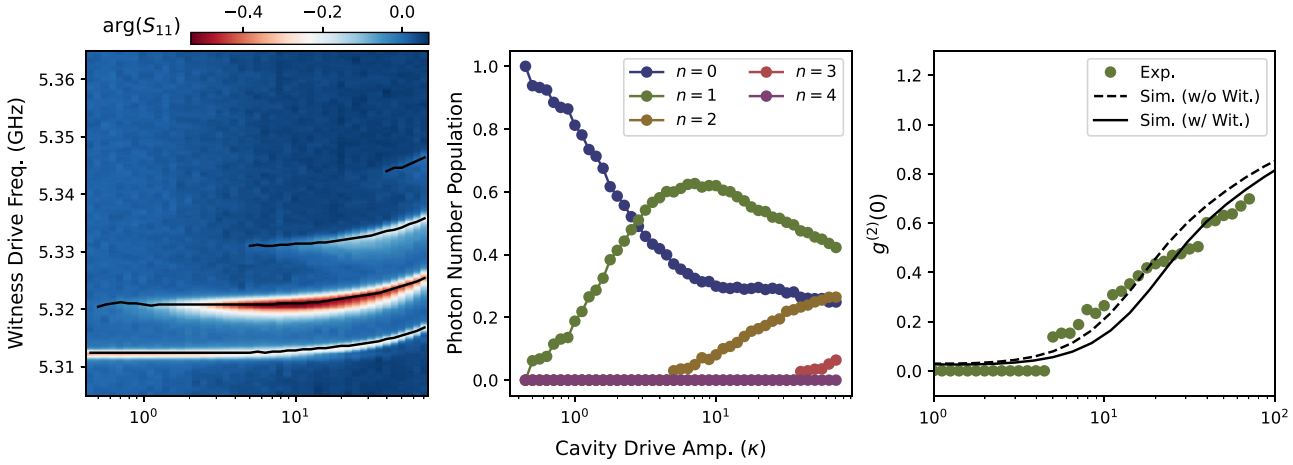



FIG. 7. Extracting $g^{(2)}(0)$ from experimental PNR spectra. (a) Sample PNR spectrum measured in the same way as Figs. 2(b)–2(e) in the main text at cavity-emitter detuning $\Delta = 2.6g$. Solid black lines overlay the data showing the extracted peak positions of the $n = 0, 1, 2, 3$ photon lines. (b) The peak prominences for each photon number, $n$, are used as weights and normalized to determine the photon-number distribution at each drive amplitude. (c) Using the formula in the text, $g^{(2)}(0)$ can be estimated from the measured photon-number distribution (blue points). This is compared to master equation simulations of the system's steady state including (solid black line) and excluding (dashed black line) the coupling of the witness qubit to the cavity.

and $\langle\sigma_z\rangle \ll 1$ (the witness qubit is weakly probed), the reflected readout tone has a phase shift $\angle S_{11} = a\Delta\langle\sigma_z\rangle = bP(n)$ proportional to the change in witness qubit population and corresponding photon-number population when the witness probe tone hits a photon-number peak.

If we exactly numerically diagonalize the full cavity-emitter-witness system, we find that

$$P_{e,n} = |\langle n-1, g, e|\psi^{g\pm}_{N,n}\rangle|^2 > 0, \tag{E4}$$

indicating that there is some residual hybridization of the witness qubit with the cavity-emitter subsystem. The eventual result of this hybridization is to reduce the inferred photon occupation $P(n)$ according to

$$P(n) \to (1 - P_{e,n})P(n). \tag{E5}$$

We can use the $P_{e,n}$ from the exact numerical diagonalization to construct a corrected estimate $g^{(2)}_{\text{corr}}(0)$. Then we find $g^{(2)}_{\text{corr}}(0) - g^{(2)}(0) \in [-0.019, 0.006], [-0.008, 0.005], [-0.019, 0.006]$ for $N = 1, 2, 3$, respectively. We include these ranges in the shaded regions of Figs. 2 and 3, but their contribution is much smaller than the error sources described below and therefore their contribution is negligible.

Next, we consider the limit on the minimum measurable $g^{(2)}(0)$ due to thermal photons occupying the cavity. At low drive amplitudes, $\eta \ll \kappa$, the cavity state is primarily a thermal state with average photon number, $n_{\text{th}}$, determined by the effective temperature of the thermal bath the cavity is in equilibrium with. The thermal state has $g^{(2)}_{\text{th}}(0) = 2$. At large drive amplitudes $\eta \gg \kappa$, the photon blockade breaks down and the system tends back toward $g^{(2)}_{\text{coh}}(0) = 1$ for a coherent state. At intermediate amplitudes there is a minimum due to the blockade and it is nonzero due to the finite nonlinearity of the Tavis-Cummings ladder and the residual thermal population in the cavity. We estimate the minimum observable $g^{(0)}(0)$ in our experiment through simulation, first minimizing $g^{(2)}(0)$ over drive amplitude at each cavity-emitter detuning, then maximizing over detuning to find a conservative, worst-case, estimate. The device is measured while mounted to the 10 mK stage of a dilution refrigerator; however, similar experiments on superconducting qubits and cavities have revealed much higher effective temperatures, typically around 50 mK [28]. Therefore, we take $T = 50$ mK in our simulations, although it is possible that the effective temperature in our system is lower, providing an even lower limit. This is plotted as a black dashed line in Figs. 2 and 3 and we find $g^{(2)}_{\text{min}}(0) < 0.043$ for $N = 1, 2, 3$ emitters, respectively. This is much lower than upper bound on $g^{(2)}(0)$ set by the other error sources.

Finally, the single largest source of error is noise in the PNR spectroscopy measurements, which limits our ability to resolve small populations in the higher photon states $n \geq 2$. Inspecting Eq. (E1), we see that uncertainty in $P(n)$ for large $n$ can lead to large errors in $g^{(2)}(0)$, particularly underestimating the true $g^{(2)}(0)$. Our approach to account for this error source is to provide an upper bound for the true value of $g^{(2)}(0)$ based on some reasonable and conservative assumptions about the system. Our full dataset extends to $\eta \approx 100\kappa$, so our first assumption is that photon-number peaks that are not observed at any cavity drive amplitude or detuning are negligibly small and can be ignored.

For photon-number peaks that are observed (up to $n = 4$) we extrapolate an upper bound to the photon population from higher amplitudes to lower amplitudes where the peak height disappears below our noise floor. A conservative way to set this upper bound is to use the scaling of a the photon populations in a coherent state where $|\alpha|$, the coherent state size, is set by the experimentally determined average photon number at a given amplitude, $|\alpha(\eta)| = \langle n \rangle$. Let $\eta_0$ be the lowest cavity drive amplitude where photon number $n$ is observable. For $\eta < \eta_0$ we upper-bound the population with

$$P(n,\eta) \leq \frac{P_{\mathrm{coh}}(n,\eta)}{P_{\mathrm{coh}}(n,\eta_0)} P(n,\eta_0), \tag{E6}$$

where

$$P_{\mathrm{coh}}(n,\eta) = \frac{\exp(-|\alpha(\eta)|^2)|\alpha(\eta)|^{2n}}{n!}. \tag{E7}$$

This amounts to assuming that the photon populations below the noise floor scale as if there is no photon blockade, which we believe is a sufficiently conservative assumption. Lastly, if the photon peak is not observed at any amplitude at a particular detuning, we take $\eta_0$ to be the maximum measured drive amplitude and $P(n,\eta_0) \to P_{\mathrm{min}}$, where $P_{\mathrm{min}}$ is the minimum resolvable photon population based on the root-mean-square noise level extracted from the PNR spectroscopy background away from all photon-number peaks.


[1] A. Imamoğlu, H. Schmidt, G. Woods, and M. Deutsch, Strongly interacting photons in a nonlinear cavity, Phys. Rev. Lett. **79**, 1467 (1997).

[2] K. M. Birnbaum, A. Boca, R. Miller, A. D. Boozer, T. E. Northup, and H. J. Kimble, Photon blockade in an optical cavity with one trapped atom, Nature **436**, 87 (2005).

[3] A. Faraon, I. Fushman, D. Englund, N. Stoltz, P. Petroff, and J. Vučković, Coherent generation of non-classical light on a chip via photon-induced tunnelling and blockade, Nat. Phys. **4**, 859 (2008).

[4] A. J. Hoffman, S. J. Srinivasan, S. Schmidt, L. Spietz, J. Aumentado, H. E. Türeci, and A. A. Houck, Dispersive photon blockade in a superconducting circuit, Phys. Rev. Lett. **107**, 053602 (2011).

[5] C. Lang, D. Bozyigit, C. Eichler, L. Steffen, J. M. Fink, A. A. Abdumalikov, M. Baur, S. Filipp, M. P. da Silva, A. Blais, and A. Wallraff, Observation of resonant photon blockade at microwave frequencies using correlation function measurements, Phys. Rev. Lett. **106**, 243601 (2011).

[6] H. Flayac and V. Savona, Unconventional photon blockade, Phys. Rev. A **96**, 053810 (2017).

[7] C. Vaneph, A. Morvan, G. Aiello, M. Féchant, M. Aprili, J. Gabelli, and J. Estève, Observation of the unconventional photon blockade in the microwave domain, Phys. Rev. Lett. **121**, 043602 (2018).

[8] M. Radulaski, K. A. Fischer, K. G. Lagoudakis, J. L. Zhang, and J. Vučković, Photon blockade in two-emitter-cavity systems, Phys. Rev. A **96**, 011801(R) (2017).

[9] R. Trivedi, M. Radulaski, K. A. Fischer, S. Fan, and J. Vučković, Photon blockade in weakly driven cavity quantum electrodynamics systems with many emitters, Phys. Rev. Lett. **122**, 243602 (2019).

[10] E. Janitz, M. K. Bhaskar, and L. Childress, Cavity quantum electrodynamics with color centers in diamond, Optica **7**, 1232 (2020).

[11] B. Lefaucher, J.-B. Jager, V. Calvo, A. Durand, Y. Baron, F. Cache, V. Jacques, I. Robert-Philip, G. Cassabois, T. Herzig, J. Meijer, S. Pezzagna, M. Khoury, M. Abbarchi, A. Dréau, and J.-M. Gérard, Cavity-enhanced zero-phonon emission from an ensemble of G centers in a silicon-on-insulator microring, Appl. Phys. Lett. **122**, 061109 (2023).

[12] S. Majety, P. Saha, V. A. Norman, and M. Radulaski, Quantum information processing with integrated silicon carbide photonics, J. Appl. Phys. **131**, 130901 (2022).

[13] M. J. Stevens, in *Single-Photon Generation and Detection*, Experimental Methods in the Physical Sciences, edited by A. Migdall, S. V. Polyakov, J. Fan, and J. C. Bienfang (Academic Press, Amsterdam, 2013), Vol. 45, pp. 25–68.

[14] M. P. da Silva, D. Bozyigit, A. Wallraff, and A. Blais, Schemes for the observation of photon correlation functions in circuit QED with linear detectors, Phys. Rev. A **82**, 043804 (2010).

[15] L. Bretheau, P. Campagne-Ibarcq, E. Flurin, F. Mallet, and B. Huard, Quantum dynamics of an electromagnetic mode that cannot contain N photons, Science **348**, 776 (2015).

[16] S. Chakram, K. He, A. V. Dixit, A. E. Oriani, R. K. Naik, N. Leung, H. Kwon, W.-L. Ma, L. Jiang, and D. I. Schuster, Multimode photon blockade, Nat. Phys. **18**, 879 (2022).

[17] A. Blais, R.-S. Huang, A. Wallraff, S. M. Girvin, and R. J. Schoelkopf, Cavity quantum electrodynamics for superconducting electrical circuits: An architecture for quantum computation, Phys. Rev. A **69**, 062320 (2004).

[18] J. Gambetta, A. Blais, D. I. Schuster, A. Wallraff, L. Frunzio, J. Majer, M. H. Devoret, S. M. Girvin, and R. J. Schoelkopf, Qubit-photon interactions in a cavity: Measurement-induced dephasing and number splitting, Phys. Rev. A **74**, 042318 (2006).

[19] D. I. Schuster, A. A. Houck, J. A. Schreier, A. Wallraff, J. M. Gambetta, A. Blais, L. Frunzio, J. Majer, B. Johnson, M. H. Devoret, S. M. Girvin, and R. J. Schoelkopf, Resolving photon number states in a superconducting circuit, Nature **445**, 515 (2007).

[20] B. Marinelli, J. Luo, H. Ren, B. M. Niedzielski, D. K. Kim, R. Das, M. Schwartz, D. I. Santiago, and I. Siddiqi, Dynamically reconfigurable photon exchange in a superconducting quantum processor, arXiv:2303.03507 [quant-ph].

[21] J. M. Fink, R. Bianchetti, M. Baur, M. Göppl, L. Steffen, S. Filipp, P. J. Leek, A. Blais, and A. Wallraff, Dressed collective qubit states and the Tavis-Cummings model in circuit QED, Phys. Rev. Lett. **103**, 083601 (2009).

[22] J. M. Fink, A. Dombi, A. Vukics, A. Wallraff, and P. Domokos, Observation of the photon-blockade breakdown phase transition, Phys. Rev. X **7**, 011012 (2017).

[23] C. Couteau, S. Barz, T. Durt, T. Gerrits, J. Huwer, R. Prevedel, J. Rarity, A. Shields, and G. Weihs, Applications of single photons to quantum communication and computing, Nat. Rev. Phys. **5**, 326 (2023).

[24] S. Pirandola, B. R. Bardhan, T. Gehring, C. Weedbrook, and S. Lloyd, Advances in photonic quantum sensing, Nat. Photonics **12**, 724 (2018).

[25] A. Rundquist, M. Bajcsy, A. Majumdar, T. Sarmiento, K. Fischer, K. G. Lagoudakis, S. Buckley, A. Y. Piggott, and J. Vučković, Nonclassical higher-order photon correlations with a quantum dot strongly coupled to a photonic-crystal nanocavity, Phys. Rev. A **90**, 023846 (2014).

[26] M. Chen, J. Tang, L. Tang, H. Wu, and K. Xia, Photon blockade and single-photon generation with multiple quantum emitters, Phys. Rev. Res. **4**, 033083 (2022).

[27] Raw data and code for plotting and QuTiP simulations, https://github.com/radulaski/PhotonBlockadeTavisCummings.

[28] F. Yan, D. Campbell, P. Krantz, M. Kjaergaard, D. Kim, J. L. Yoder, D. Hover, A. Sears, A. J. Kerman, T. P. Orlando, S. Gustavsson, and W. D. Oliver, Distinguishing coherent and thermal photon noise in a circuit quantum electrodynamical system, Phys. Rev. Lett. **120**, 260504 (2018).